

**TELESCOPE SCIENTIST ON THE ADVANCED X-RAY ASTROPHYSICS
OBSERVATORY**

NASA Grant NAG8-1607

Annual Report

For the Periods 1 October 2001 through 30 September 2002

Principal Investigator
Dr. L. Van Speybroeck

November 2002

Prepared for:

National Aeronautics and Space Administration
George C. Marshall Space Flight Center
Marshall Space Flight Center, Alabama 35812

Smithsonian Institution
Astrophysical Observatory
Cambridge, Massachusetts 02138

The Smithsonian Astrophysical Observatory
is a member of the
Harvard-Smithsonian Center for Astrophysics

The NASA Technical Officer for this grant is Carl M. Smith, Code FD03, NASA, George C. Marshall Space Flight Center, Marshall Space Flight Center, Alabama 35812.

100

100

100

100

100

100

100

100

100

100

100

100

100

100

100

100

100

100

100

100

100

100

100

100

100

100

100

100

100

100

100

100

100

100

100

100

100

100

100

100

100

100

100

100

100

Semiannual and Annual Reports

NASA Grant NAG8-1607

AXAF Telescope Scientist

Period of Performance: 1 October 2001 through 31 September 2002

1. Introduction.

This period included many scientific observations made with the Chandra Observatory. The results, as is well known, are spectacular. Fortunately, the HRMA performance continues to be essentially identical to that predicted from ground calibration data. The Telescope Scientist Team has improved the mirror model to provide a more accurate description to the Chandra observers and enable them to reduce the systematic errors and uncertainties in their data reduction. We also have made considerable progress in improving the scattering model.

There also has been progress in the scientific program. At this time 58 distant clusters of galaxies have been observed. We are performing a systematic analysis of this rather large data set for the purpose of determining absolute distances utilizing the Sunyaev Zel'dovich effect. These observations also have been used to study the evolution of the cluster baryon mass function and the cosmological constraints which result from this evolution.

2. Chandra Mirror Activities

2.1. Monitoring and Program Support

We continued to monitor the HRMA mirror performance in flight; during this period we did not find it necessary to update the basic mirror parameters or ray tracing models as a result of changes in flight performance. We contributed to NASA's Chandra AO4 Research Announcement. We rewrote and updated the HRMA chapter of the "Chandra Proposers' Observatory Guide", which was sent to all the Chandra proposers with the NASA's Chandra AOs. We also worked with CXC optical group for the ray-trace analysis, with the Chandra user support group to provide information needed for the Chandra users, and with the CXC data center to provide information for the CIAO database.

2.2. Scattering

We continued our study of X-ray scattering from random rough surfaces, and established a new scattering model.

The theory of scattering from random rough surfaces has been the subject of a number of books and many research papers. The modeling of X-ray scattering at grazing angles is difficult because of its short wavelength and the small angle between the wave and the surface. Almost all the current approaches use a common approximation – the scattering angle is much smaller than the grazing incident angle. Most of the approaches also ignore the scattering asymmetry around the direction of specular reflection (scattering towards vs. away from the surface). Many of the present models also are limited to small perturbations of the ideal surface. These approximations are not adequate for many of the applications involving X-ray mirrors.

To fully evaluate the Chandra performance and analyze the scientific data, we need an accurate model of the X-ray scattering. Our new method models the X-ray scattering directly from first principles. An actual rough surface is (incompletely) described by its Power Spectral Density (PSD). For a given PSD, model surfaces with the same roughness as the actual surface are constructed by preserving the PSD amplitudes and assigning a random phase to each spectral component. Rays representing the incident wave are reflected from the model surface and projected onto a flat plane, which approximates the model surface, as outgoing rays and corrected for phase delays. The projected outgoing rays are then corrected for wave densities and redistributed onto an uniform grid where the model surface is constructed. The scattering is then calculated by taking the Fast Fourier Transform (FFT) of the resulting distribution.

Our new method treats the reflection and scattering together, and consequently both depend upon the surface roughness. It does not require the approximation that the scattering angle is small compared to the grazing angle so that all the scattered rays can be traced accurately. This method is generally applicable. We have applied this method to the mirrors of the Chandra X-ray Observatory and have shown that the calculated scattering profile is as expected, including the Fraunhofer scattering patterns which result from the finite length of the surfaces.

This work is still continuing. Next we will generate scattering tables, which are the tabulations of the scattering function \mathcal{S} . Then we will use these scattering tables in our ray-trace model to simulate the CXO performance and compare it with the real results of the CXO, from both on-orbit observations and its ground calibrations. This method should be useful for other X-ray telescope missions as well.

We have presented this work at the SPIE '02 meeting. The paper describing this new method is published in the SPIE proceedings 4851-11 and is included as appendix A of this report.

3. The Funtools Project

The Funtools project arose out of conversations with astronomers about the decline in their software development efforts over the past decade. A stated reason for this decline is that it takes too much effort to master one of the existing FITS libraries simply in order to write a few analysis programs. This problem is exacerbated by the fact that astronomers typically develop new programs only occasionally, and the long interval between coding efforts often necessitates re-learning the FITS interfaces.

As stated in our proposal for this past year, software development plans for the funtools software suite and the xpa messaging system covered the following areas:

- Closer integration of funtools with the ds9 image display program.
- Enhanced security of funtools and xpa code.
- Development of firewall support in xpa.

- Provide elliptical and rectangular annuli support for funtools region masks.

In all four areas we accomplished significant advances:

1. A graphical parameter interface was developed in ds9 to support user-specified inputs to analysis routines. Macro expansion of funtools command lines also was enhanced so that various internal ds9 values could easily be passed to the funtools programs. As a result, funtools programs now are routinely executed from within ds9. These enhancements were released in ds9 version 2.1 in April 2002.

2. Code security was enhanced for both funtools and xpa. The insecure Unix system() function was replaced by our secure launch() routine. The latter explicitly utilizes fork()/exec() instead of "sh -c" and thus is not susceptible to the usual shell-based attacks. The insecure Unix mktemp() routine was replaced by our secure mkrtemp() routine. The latter makes a unique temporary filename that is hard to guess and optionally opens it using secure flags that prevent race conditions. These enhancements were released in funtools version 1.2 in April 2002.

3. The xpa system now supports communication through firewalls. Using the new xparemote command, a local xpa-enabled program such as ds9 can register itself with a remote xpans name server set in xpa proxy mode. The local ds9 can then receive data and commands from behind a port-blocking firewall, since the socket connection is made securely from inside the firewall to the xpans on the outside. Network address translation (NAT) schemes also are handled properly. These enhancements were released in xpa version 2.1 in April 2002.

4. Elliptical and rectangular annuli regions were added to funtools/ds9 spatial masks. The panda (Pie AND Annulus) shape also was extended to ellipses and boxes. The syntax for these commands is shown below:

```

BOX      xcenter ycenter xw1 yh1 xw2 yh2 ... xwn yhn (angle)
BOX      xcenter ycenter xwlo yhlo xwhi yhhi n=[number] (angle)
ELLIPSE  xcenter ycenter xw1 yh1 xw2 yh2 ... xwn yhn (angle)
ELLIPSE  xcenter ycenter xwlo yhlo xwhi yhhi n=[number] auto(angle)
BPANDA   xcen ycen ang1 ang2 nang xwlo yhlo xwhi yhhi nrad (ang) # box
EPANDA   xcen ycen ang1 ang2 nang xwlo yhlo xwhi yhhi nrad (ang) # ellipse

```

These enhancements were first released in beta test versions of funtools starting in September 2002.

For general information on xpa and funtools (including download information), please see: <http://hea-www.harvard.edu/RD/xpa/index.html>
<http://hea-www.harvard.edu/RD/funtools/index.html>

4. Science Program.

The Telescope Scientist guaranteed time is devoted to observations of distant galaxy clusters to study their evolution and to determine cosmological scale quantities using the Sunyaev Zel'dovich effect. Cooperative agreements with other scientists, including radio

observers, have been formed. Preliminary data processing has been performed upon the 58 data sets received at this time. This processing includes correction for the changes in the ACIS gain, the identification and elimination of periods of high background, the removal of ACIS after-glow effects, the calculation of exposure maps and images, and the search for serendipitous sources. The superior angular resolution of Chandra shows more structure in galaxy cluster systems than we had expected based upon pre-Chandra observations; this significantly complicates the final data analysis.

The different sensitivity of the radio and X-ray measurements to the outer parts of the cluster contributes to a basic uncertainty in the analysis of these data for the purpose of determining distances. We have begun a program of simulations of the X-ray and radio data to determine the sensitivity of the final results to the relatively poorly measured low surface brightness regions at large cluster radii.

One very important result already has been obtained, and is in the process of final preparation for publication by Vikhlinin et al. We find that the cluster density for equivalent baryon masses strongly evolves between redshifts of 0.4-0.8 and the present epoch; the local density of mass clusters per unit co-moving volume is approximately 10 times that found at redshifts of 0.5. The density evolution is a strong function of the cosmological parameters Ω and Λ . We find that the band in these parameters allowed by cluster evolution is comparable in scale to the bands allowed by SN Ia and the CMB, and that all three bands intersect in a small region near the currently commonly used values of $\Omega = 0.3$, $\Lambda = 0.7$. This may either be viewed as strong supporting evidence that there are not important systematic errors in the interpretation of the three types of data, or, if we accept the cosmological parameters as determined from the SN Ia and CMB data, then we have strong supporting evidence for models of cluster formation.

Dr. Ping Zhao continued the study of stellar black holes. This includes the search for new black holes and the study of known black holes. Dr. Zhao is a principal investigator of a program to monitor the quiescent black hole X-ray novae (BHXN), and also is a principal investigator of a program to search for quiescent X-ray novae among the old optical novae.

Dr. Zhao also is a co-investigator of the Chandra Multiwavelength Plane Survey Project (ChAMPlane) which is a project to identify a large sample of serendipitous X-ray sources in the galactic plane Chandra fields, in order to determine the populations of accretion-powered binaries in the Galaxy. He has supported these studies with optical observations using the MMT and Magellan telescopes.

A. Paper on X-ray Scattering Published in 2002 SPIE 4851-11

A new method to model X-ray scattering from random rough surfaces

Ping Zhao and Leon P. Van Speybroeck

Harvard-Smithsonian Center for Astrophysics
60 Garden Street, Cambridge, MA 02138 U.S.A.

ABSTRACT

This paper presents a method for modeling the X-ray scattering from random rough surfaces. An actual rough surface is (incompletely) described by its Power Spectral Density (PSD). For a given PSD, model surfaces with the same roughness as the actual surface are constructed by preserving the PSD amplitudes and assigning a random phase to each spectral component. Rays representing the incident wave are reflected from the model surface and projected onto a flat plane, which approximates the model surface, as outgoing rays and corrected for phase delays. The projected outgoing rays are then corrected for wave densities and redistributed onto an uniform grid where the model surface is constructed. The scattering is then calculated by taking the Fast Fourier Transform (FFT) of the resulting distribution. This method is generally applicable and is not limited to small scattering angles. It provides the correct asymmetrical scattering profile for grazing incident radiation. We apply this method to the mirrors of the Chandra X-ray Observatory and show the results. We also expect this method to be useful for other X-ray telescope missions.

Keywords: X-ray scattering, random rough surface, X-ray mirror, X-ray telescope, Chandra X-ray Observatory

1. INTRODUCTION

The study of scattering from random rough surfaces goes back at least to Rayleigh in 1887,¹ and has been investigated by many physicists and engineers. The problem has been the subject of numerous books, including the classic "The Scattering of Electromagnetic Waves From Rough Surfaces" by Beckmann and Spizzichino² and countless research papers.³ Many people have also studied X-ray scattering at grazing angles as part of this subject. This problem is even more difficult because of the short wavelength (compared to the scale of the surface roughness) and the small angle between the wave propagation direction and the surface. Most approaches in the literature make the approximation that the scattering angle is much smaller than the incident grazing angle. Some of the treatments use the approximation that the surfaces are sufficiently "smooth" so that a low order expansion in the surface height errors is adequate, and consequently are limited in their applications. Many of the approaches can not obtain the scattering asymmetry around the direction of specular reflection (scattering towards vs. away from the surface). These approximations are not adequate for many of the applications involving X-ray mirrors.

This new study of the century old problem is motivated by our direct involvement of the evaluation of the X-ray mirror performance aboard the Chandra X-ray Observatory (CXO) – the NASA's third great space observatories now have been successfully operated for three years and have brought us fruitful scientific results with many exciting discoveries. A major achievement of the CXO compared to previous X-ray missions is its unprecedented spatial resolution ($< 0.5''$ FWHM). This is mainly due to the design and manufacture of its X-ray mirrors. These mirrors are the largest, most precise grazing incidence optics ever built. At 0.84-m long and 0.6 – 1.2-m in diameters, the surface area of each mirror ranging from 1.6 to 3.2 square meters. They were polished to the highest quality ever achieved for any X-ray mirrors of this size. The surface roughness of these mirrors is comparable to or less than the X-ray wavelengths in the 0.1–10 keV band over most of the mirror surfaces.

Further author information: Ping Zhao: E-mail: zhao@cfa.harvard.edu

However, the mirrors are not perfect, and consequently there are still small amount of scattered X-rays. We need an accurate model of the X-ray scattering to fully evaluate the CXO performance and analyze the scientific data. We have built a raytrace computer model to simulate the CXO performance. In the current raytrace model, the reflection and scattering are treated as separate effects. Each ray hit the mirror is reflected according the reflectivity of the surface geometry and the low frequency surface map, but not the high frequency roughness, therefore the effect of the surface roughness on the reflection efficiency is lost. The scattering is treated with small (scattering) angle approximation.

Our new method treats the reflection and scattering together, and consequently both depend upon the surface roughness. It does not require the approximation that the scattering angle is small compared to the grazing angle so that all the scattered rays can be traced accurately.

2. POWER SPECTRAL DENSITY OF ROUGH SURFACES

A rough surface is described, statistically, by its surface Power Spectral Density (PSD) as a function of the surface spatial frequency, f . Consider a 1-dimensional surface with length L and surface height (i.e. deviation from a perfectly flat surface): $z = h(x)$, which assumes the value z ($-\infty < z < \infty$). Its PSD is defined as:^{*}

$$PSD(f) \equiv 2W_1(f) = \frac{2}{L} \left| \int_{-L/2}^{L/2} e^{i2\pi x f} h(x) dx \right|^2 \quad (1)$$

The PSD, as it is defined, is the “spectrum” of the surface roughness. Its value at f is simply the “power” at that frequency. It is easy to distinguish between periodic and random rough surfaces from their PSDs. For periodic rough surfaces, there are some “spectral lines” in their PSDs; while these lines don’t exist for a real random rough surface.

Given a PSD function $2W_1$, the surface roughness amplitude RMS in the frequency band of $f_1 - f_2$ (both f_1 and f_2 are positive) can be calculated as:

$$\sigma_{f_1-f_2}^2 = \int_{f_1}^{f_2} 2W_1(f) df \quad (2)$$

3. CHANDRA X-RAY OPTICS

The Chandra X-ray optics – High Resolution Mirror Assembly (HRMA) – is an assembly of four nested Wolter Type-I (paraboloid and hyperboloid) grazing incidence mirrors made of Zerodur and coated with iridium (Ir).⁴⁻⁶ The mirror elements were polished by Hughes Danbury Optical Systems, Inc. (HDOS) in Danbury, CT. The surface roughness was measured during the HDOS metrology measurements after the final polishing, but before the iridium coating.⁷ Tests conducted on sample flats before and after the coating indicate that the coating does not change the surface roughness.

The instruments used for the measurements were the Circularity and Inner Diameter Station (CIDS), the Precision Metrology Station (PMS), and the Micro Phase Measuring Interferometer (MPMI, aka WYKO). The CIDS was used to determine the circularity and the inner diameters. The PMS was used to measure along individual axial meridians. With these two instruments, HDOS essentially measured the ‘hoops’ and ‘staves’ of each mirror barrel, and thus mapped the entire surface. The micro-roughness was sampled along meridian at different azimuths using the WYKO instrument at three different magnifications ($\times 1.5$, $\times 10$ & $\times 40$).^{7,8}

These metrology data were Fourier transformed and filtered. The low frequency parts of the CIDS and PMS data were used to form mirror surface deformation (from the designed mirror surface) maps. The high frequency parts of the PMS data and the WYKO data were used to estimate the surface micro-roughness. Both of them are parts of the HRMA model we built for the raytrace simulation of the Chandra performance.

^{*}The definition $2W_1$ is conventional, where the subscript ₁ denotes 1-dimensional; the PSD satisfies $PSD(-f) = PSD(f)$, and typically positive frequency limits are used for most spectral integrals. The total power, σ^2 , is the integral of $2W_1$ from $f = 0$ to ∞ , i.e. $\sigma^2 = \int_0^\infty 2W_1(f) df$.

Table 1. HRMA Mirror Sections and Their Surface Roughness

HRMA Mirror	Sections											Num of Sections
	Surface Roughness Amplitude RMS $\sigma_{1-1000/\text{mm}}$ (Å)											
P1	LC	LB	LA	M (88%)	SA	SB	SC					7
	50.3	8.49	4.51	3.58	4.91	5.94	53.9					
P3		LB	LA	M (92%)	SA	SB						5
		5.37	5.26	1.96	2.38	4.83						
P4		LB	LA	M (93%)	SA	SB						5
		6.41	3.15	2.57	3.21	6.81						
P6		LB	LA	M (94%)	SA	SB						5
		37.1	5.23	3.34	5.65	20.9						
H1	LD	LC	LB	LA	M (88%)	SA	SB	SC	SD	SE	SF	11
	26.9	5.34	3.64	3.34	3.32	3.32	3.32	3.32	3.53	7.30	60.3	
H3		LC	LB	LA	M (92%)	SA	SB	SC	SD			8
		4.87	2.90	2.23	2.08	2.08	2.10	3.95	5.56			
H4	LD	LC	LB	LA	M (93%)	SA	SB	SC	SD	SE		10
	7.18	3.83	2.61	2.57	2.36	2.36	2.74	2.68	4.01	29.4		
H6	LD	LC	LB	LA	M (94%)	SA	SB	SC	SD	SE		10
	19.0	4.92	2.51	2.23	1.95	1.95	1.95	2.07	2.96	15.9		
Total												61

The mirror surface micro-roughness has little variation with azimuth, but tends to become worse near the mirror ends. We divided the data for each mirror into several axial sections which were selected so that the measured roughness at several places within a section were reasonably uniform; this resulted in a total of 61 sections. We then averaged the PSD measurements within each section to provide an estimate of the PSD for that portion of the mirror element. Table 1 shows the resulting surface roughness in the 61 HRMA mirror sections. The eight mirrors are named P1,3,4,6 (paraboloid) and H1,3,4,6 (hyperboloid) due to historical reasons (there were 6 mirror pairs when the HRMA was designed). The number underneath each section name is the surface roughness amplitude RMS, $\sigma_{1-1000/\text{mm}}$, calculated according to Eq. (2) for $f = 1 - 1000 \text{ mm}^{-1}$. Each mirror is 838.2 mm in length. The middle sections (M), which are the best polished and hence have the lowest PSDs, cover most part of the mirror surface (the number in parentheses after each M denote the percentage coverage). The σ 's for the M sections are only 2-3 Å. The end sections, where the σ 's are relatively higher, cover a very small part of the mirror (< 1%), and hence contribute very little to the mirror performance.

Figures 1 and 2 show the PSDs of the M (middle) and SC (small end) sections of P1. P1 and H1 were the first polished mirror pair and are slightly "rougher" than other pairs (see Table 1). The dash and dotted lines show the data from different measurements: the PMS data are in the low frequency range ($f = 0.001 - 0.3 \text{ mm}^{-1}$); the WYKO data with 3 magnifications are in the higher frequency range ($f = 0.3 - 1000 \text{ mm}^{-1}$). The solid line is the combined PSD from all four frequency ranges. The SC section obviously is much rougher than the M section.

4. MODEL SURFACES

Typically, a random rough surface is only described by its PSD. Most of the methods calculate the scattering from the surface PSD. However, our method calculates the scattering directly from the surface high frequency spatial profile. Therefore, we first need to construct a model surface that is consistent with a given PSD. From a random rough surface profile, one can derive a unique PSD. But from a given PSD one can't construct the original surface, because the phase information was lost when deriving the PSD. However, one can construct many model surfaces with the same roughness as the original one from the given PSD by assigning different random phase factors to the spectral component.

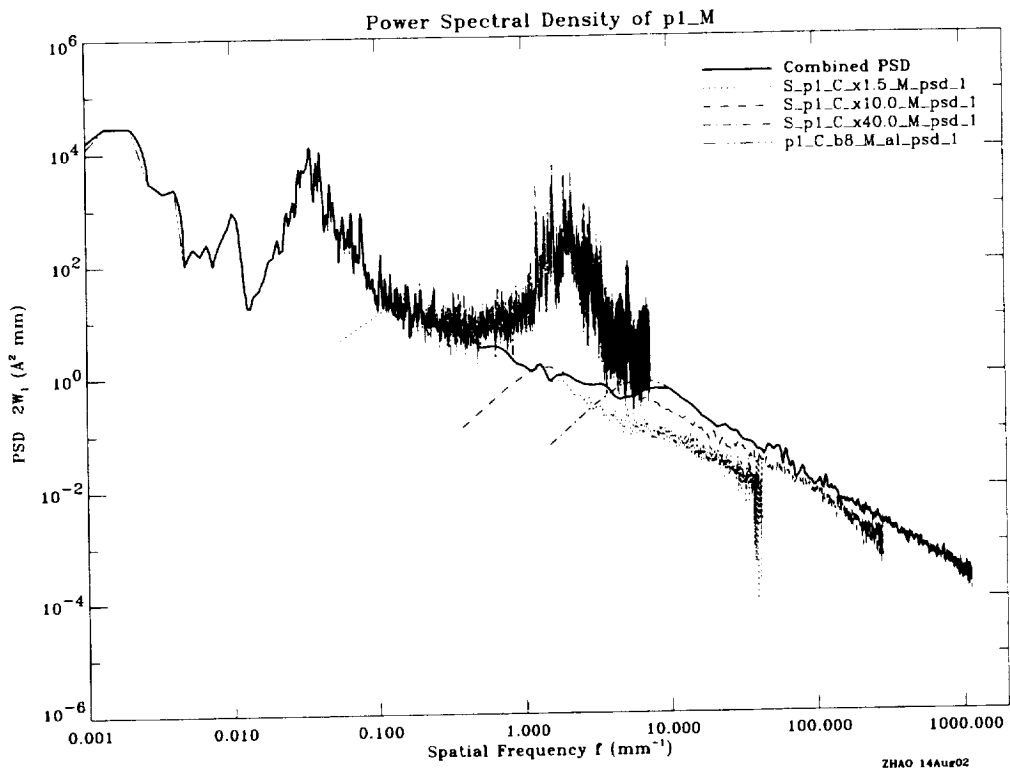


Figure 1. Surface PSD of Chandra mirror P1-M, the middle section of mirror P1.

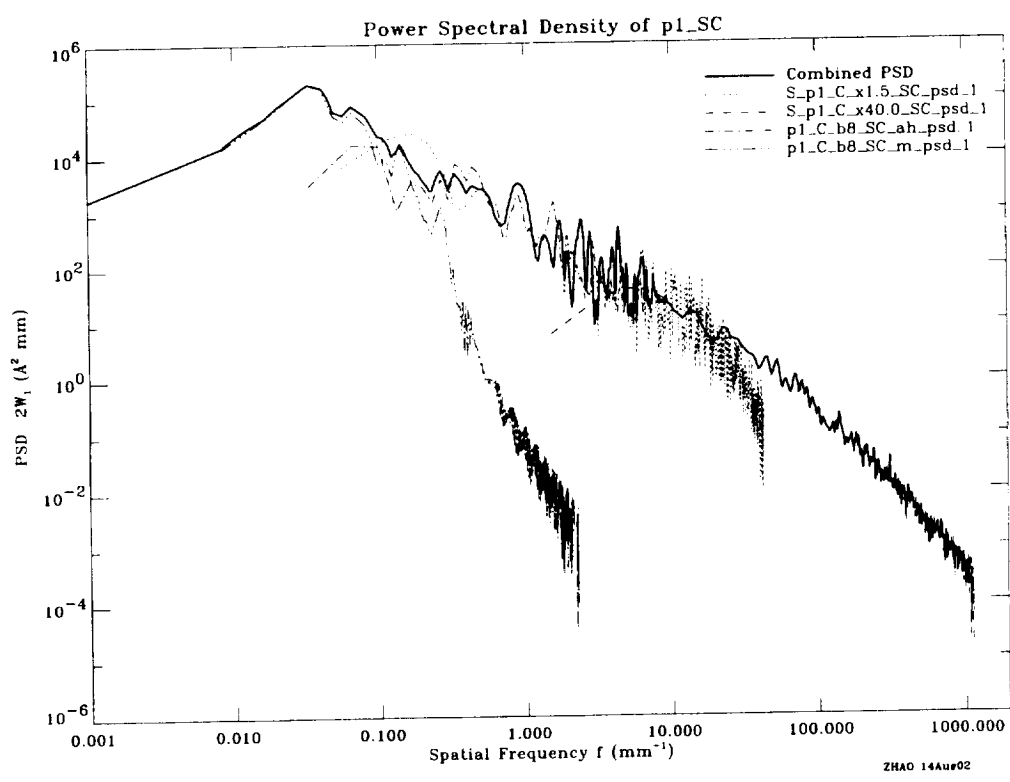


Figure 2. Surface PSD of Chandra mirror P1-SC, the small end section of mirror P1.

To construct a 1-dimensional model surface with length L , we need to obtain N consecutive surface height values $h_i = h(x_i)$ with a fixed interval Δx to cover the surface (i.e. $N\Delta x = L$), and its surface tangent values $h'_i = h'(x_i)$. In Appendix A, we show that h_i and h'_i can be computed from the surface PSD using the following Fourier transforms:

$$h_i = \frac{1}{N} \sum_{j=-(N/2-1)}^{N/2} H_j e^{-i\frac{2\pi ij}{N}} \quad (3)$$

$$h'_i = \frac{1}{N} \sum_{j=-(N/2-1)}^{N/2} (-i2\pi f_j H_j) e^{-i\frac{2\pi ij}{N}} \quad (4)$$

where $H_j = N\sqrt{\frac{PSD(f_j)\Delta f}{2}} e^{i\varphi_j}$, φ_j is the assigned random phase factor, and $\Delta f = 1/N\Delta x$. Both h_i and h'_i are real, this requires $H_{-j} = H_j^*$, i.e. $PSD(f_{-j}) = PSD(f_j)$ and $\varphi_{-j} = -\varphi_j$.

To construct the model surfaces of HRMA, we choose $N = 2^{21}$ and $\Delta x = 0.0004$ mm. So $L = N\Delta x = 838.86$ mm, and $\Delta f = 1/N\Delta x = 0.001192$ mm⁻¹. Figures 3 and 4 show one set of model surface sections P1-M and P1-SC, constructed using Eqs. (3) and (4) with these parameters.

5. SCATTERING FROM MODEL SURFACES

In this section, we calculate the scattering of plane incident waves from a surface model; most of the detailed derivations of the formulae can be found in Appendices B and C.

We assume that the surfaces are sufficiently smooth so that: 1) there is no shadowing of one part of the surface by another; and 2) there is no reflection from one part of the surface to another, i.e. there are no multiple reflections by the same surface. For an incident plane wave with grazing angle θ_1 , the first condition requires that the absolute values of all the surface tangents, $|h'_i|$, are less than θ_1 . The second condition requires $|h'_i|$ less than $\theta_1/2$ (when $h'_i = -\theta_1/2$, the reflected wave is parallel to the surface). The first condition is automatically satisfied when the second condition is met. So the surface smoothness condition for applying this method is:

$$|h'_i| < \frac{\theta_1}{2} \quad (5)$$

This condition is easily satisfied for all 61 sections of the HRMA, as can be seen by comparing the tangent distributions in Figures 3 and 4 with the mean grazing angles of the four shells (51.26', 41.27', 36.43', 27.08'),

The scattering in the transverse direction, i.e. the off-plane scattering, is smaller than that in the plane of incidence by approximately a factor of the grazing angle, and consequently is less than the uncertainties in our surface PSD. Therefore, in this paper, we ignore the off-plane scattering and limit our discussion to a 1-dimensional surface.

The scattering formula is given by the discrete Fourier transform of the field on the flat surface S_0 , as shown in Eq. (58) in Appendix C:

$$I(\theta_{j+q/p}) = \mathcal{A} \left(\frac{\Delta x \sin(\theta_1 - \theta_{j+q/p})}{\lambda} \right)^2 \left| \sum_{i=-(N/2-1)}^{N/2} \left(\mathbf{E}_i e^{i\frac{2\pi iq/p}{N}} \right) e^{i\frac{2\pi ij}{N}} \right|^2 \quad (q = 0, 1, \dots, p-1) \quad (6)$$

where the scattering intensity I is a function of the scattering angle $\theta_{j+q/p}$, which is the deviation from the specular reflection direction towards the surface; λ is the wavelength; \mathbf{E}_i is the field amplitude, after the reflection, on the flat surface at the uniform grid x_i where the model surface was constructed. As described in Appendix C.3, \mathbf{E}_i is a function of the incident wave, the model surface height and tangent, and the local reflectivity. \mathcal{A} is a normalization factor given by Eq. (63). Again we choose $N = 2^{21}$ to use the entire length of the model surface for the FFT computation.

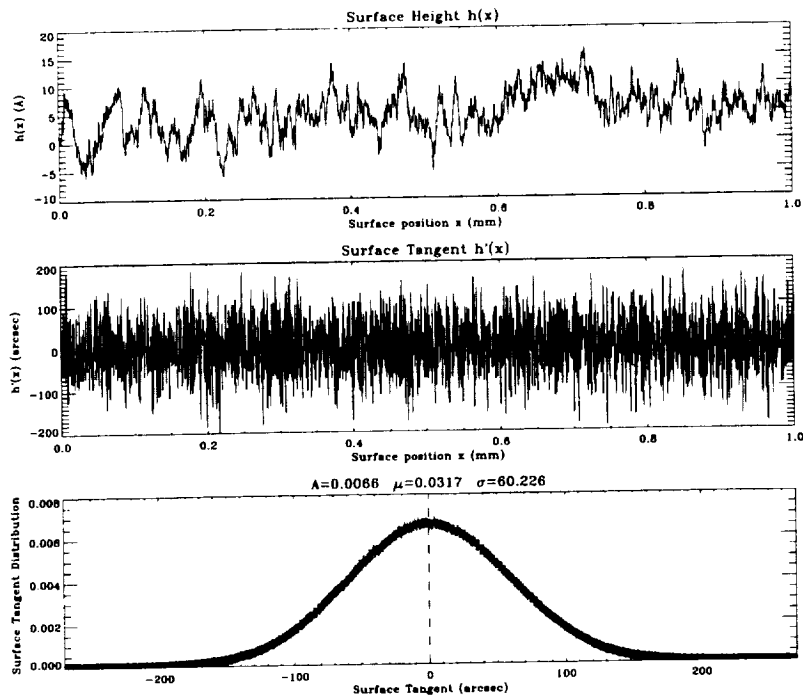


Figure 3. A model surface of Chandra mirror section P1-M, which covers 88% of the mirror P1. The top two panels show the surface height and the surface tangent for a 1 mm section of the model mirror. The bottom panel shows the surface tangent distribution of the entire surface, which can be described accurately by a Gaussian with $\sigma = 60.2''$.

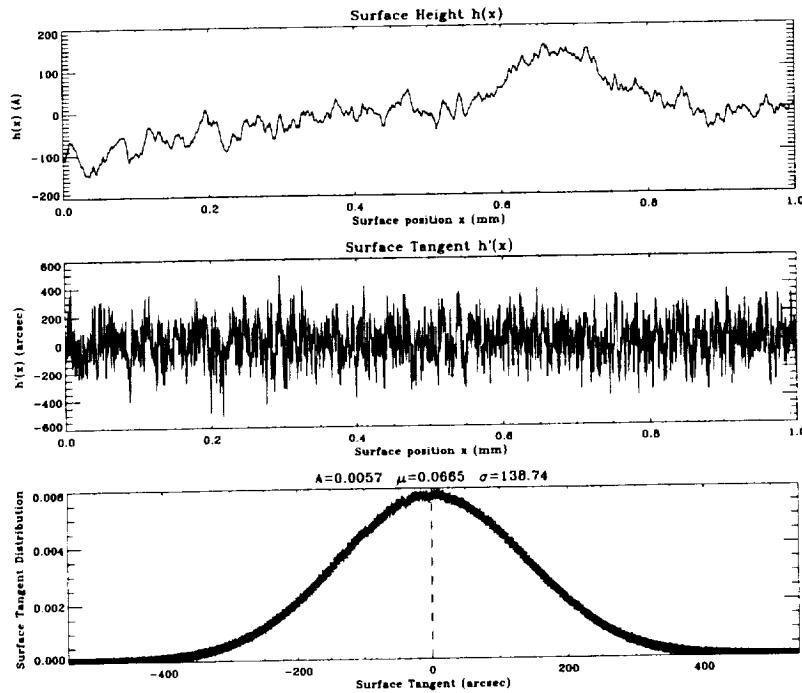


Figure 4. A model surface of Chandra mirror section P1-SC, which is the “worst” end-section of the P1 mirror. The top two panels show the surface height and the surface tangent for a 1 mm section of the model mirror. The bottom panel shows the surface tangent distribution of the entire surface, which can be described accurately by a Gaussian with $\sigma = 138.7''$.

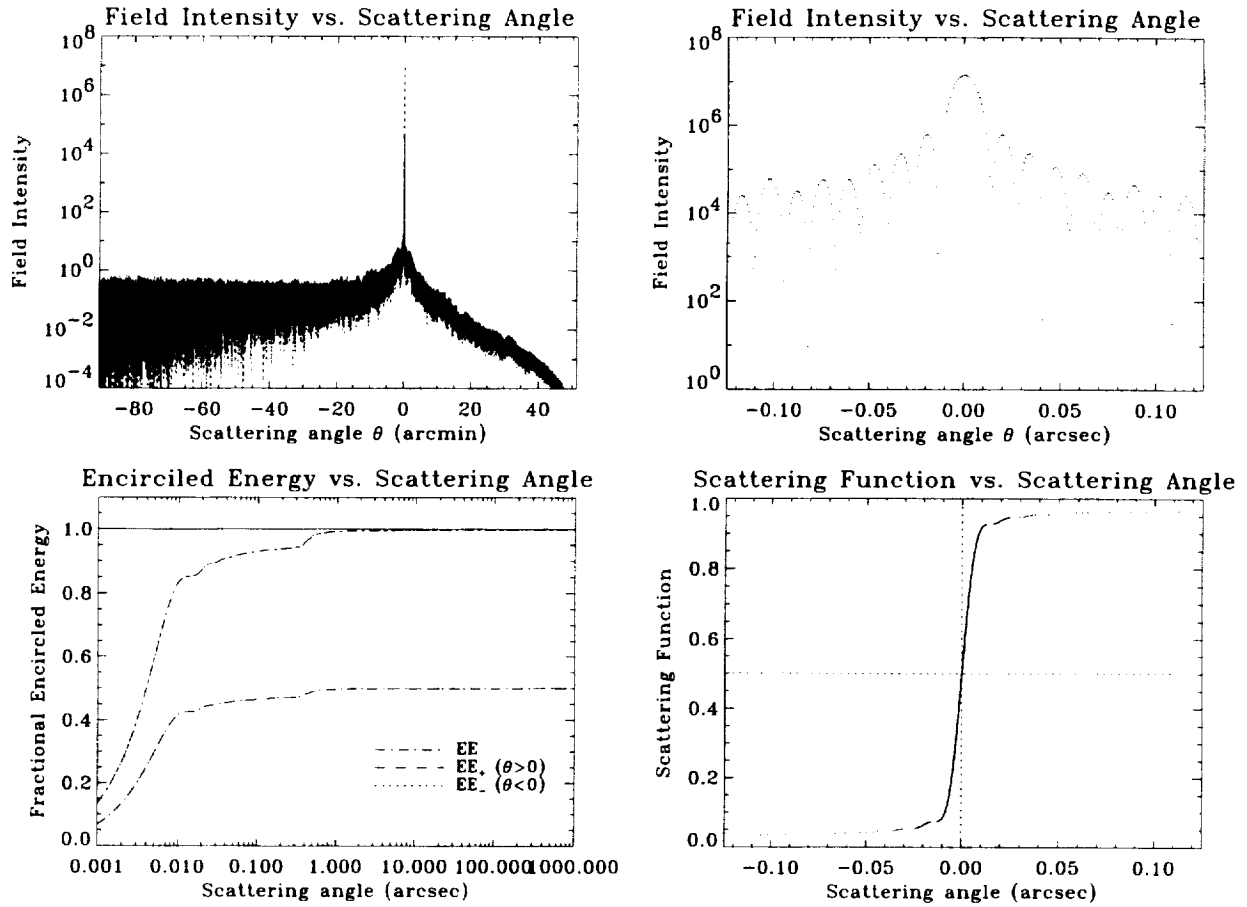


Figure 5. The scattering of 1.49 keV X-rays at $51.26'$ grazing incident angle from the model surface P1-M. The top-left panel shows the scattering field intensity versus the scattering angle. The very sharp peak is at the specular reflection direction $\theta = 0$. The asymmetric nature of the scattering is clearly shown. The top-right panel is the same plot but zoomed into the core of the peak; it shows the Fraunhofer diffraction pattern due to the finite mirror length. The bottom-left panel shows the fractional Encircled Energy (EE) versus the scattering angle, for both sides of the specular direction, and also their sum. The bottom-right panel shows the scattering function S versus the scattering angle in the same range as the top-right panel.

Figures 5 and 6 show the scattering results for 1.49 keV X-rays incident upon the mirror P1 at its mean grazing angle ($51.26'$). The top two panels show the scattering field intensity versus the scattering angle. The sharp peak of specular reflection (top-left) and the Fraunhofer diffraction pattern (top-right) are shown as expected. The bottom two panels show the fractional Encircled Energies EE_+ , EE_- , EE and the scattering function S defined as:

$$EE_+(\theta) \equiv \frac{1}{\mathcal{E}_s} \int_0^\theta I(\theta) d\theta = \frac{1}{\mathcal{R} \mathcal{E}_i} \int_0^\theta I(\theta) d\theta \quad (7)$$

$$EE_-(\theta) \equiv \frac{1}{\mathcal{E}_s} \int_{-\theta}^0 I(\theta) d\theta = \frac{1}{\mathcal{R} \mathcal{E}_i} \int_{-\theta}^0 I(\theta) d\theta \quad (8)$$

$$EE(\theta) \equiv \frac{1}{\mathcal{E}_s} \int_{-\theta}^\theta I(\theta) d\theta = \frac{1}{\mathcal{R} \mathcal{E}_i} \int_{-\theta}^\theta I(\theta) d\theta \quad (9)$$

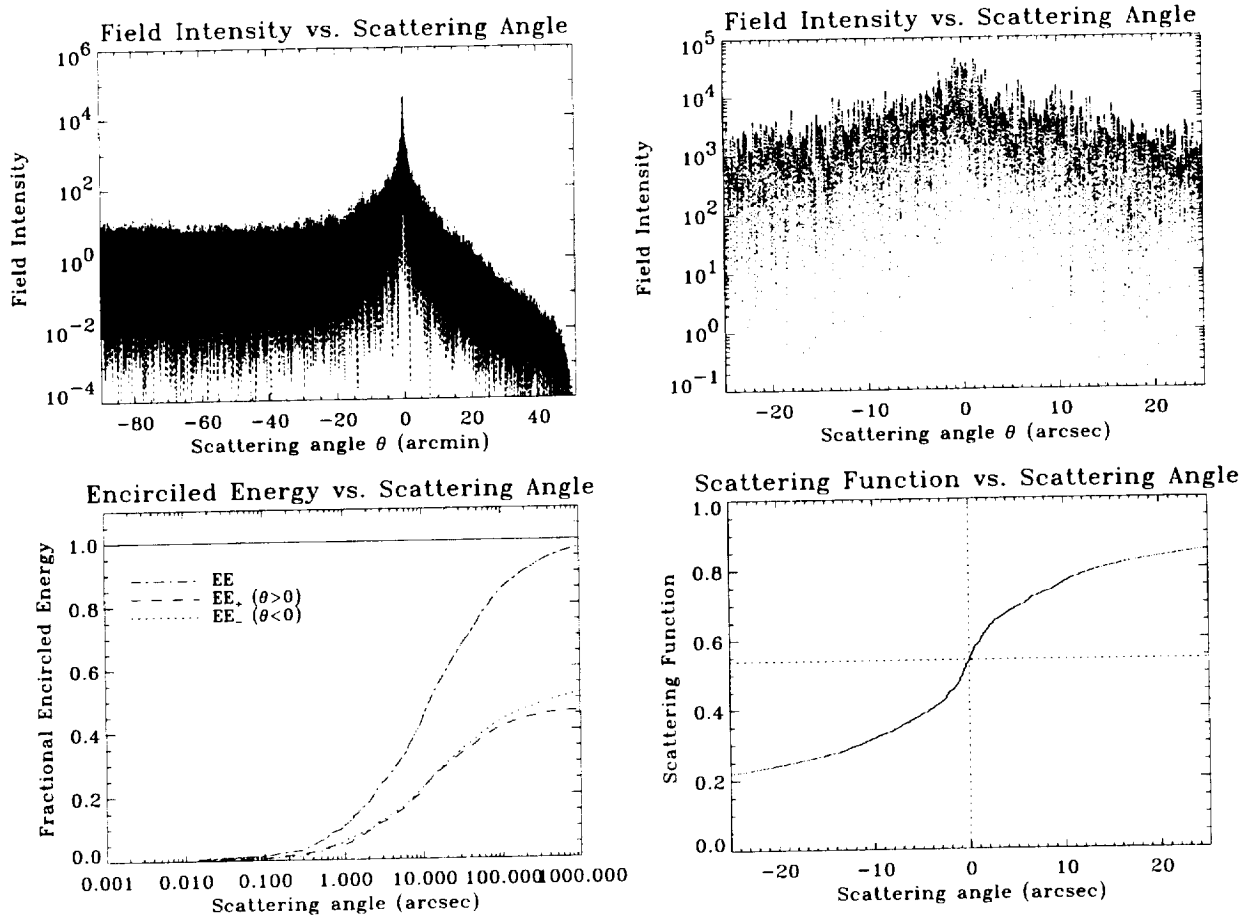


Figure 6. Scattering from model surface P1-SC. It has much broader scattering peak than P1-M.

$$S(\theta) \equiv \frac{1}{\mathcal{E}_s} \int_{-\infty}^{\theta} I(\theta) d\theta = \frac{1}{\mathcal{R} \mathcal{E}_i} \int_{-\infty}^{\theta} I(\theta) d\theta \quad (10)$$

where \mathcal{E}_i , \mathcal{E}_s and \mathcal{R} are the total incident and scattered energy, and the reflectivity of the rough surface as described in Appendix C.5.

6. SUMMARY AND FUTURE WORK

We have developed a method to model the wave scattering from random rough surfaces. Model surfaces with the same roughness as the actual surface are constructed from the actual PSD. The scattering from the model surfaces is calculated using the scattering formulae we derived in this paper. These scattering formulae are based on the general Kirchhoff equations but without small angle approximations. This method treats the reflection and scattering together and provides the dependence of the reflectivity on the surface roughness. It is applicable in general and is especially useful for X-ray scattering at grazing angles. We have applied this method to the mirrors of the Chandra X-ray Observatory and have shown that the calculated scattering profile is as expected, including the Fraunhofer scattering patterns which result from the finite length of the surfaces.

This work is still continuing. Next we will generate scattering tables, which are the tabulations of the scattering function S . Then we will use these scattering tables in our raytrace model to simulate the CXO performance and compare it with the real results of the CXO, from both on-orbit observations and its ground calibrations. This method should be useful for other X-ray telescope missions as well.

APPENDIX A. CONSTRUCTION OF MODEL SURFACES

A.1. Fourier Transform

The **Continuous Fourier Transform** equations are⁹:

$$H(f) = \int_{-\infty}^{\infty} h(x) e^{i2\pi x f} dx \quad (\text{forward}) \quad (11)$$

$$h(x) = \int_{-\infty}^{\infty} H(f) e^{-i2\pi x f} df \quad (\text{inverse}) \quad (12)$$

Here if h is a function of position, x , in mm, H will be a function of spatial frequency, f , in mm^{-1} .

When there are N consecutive sampled values at $x = x_i$ with the sampling interval Δx , we make the transform:

$$x \Rightarrow x_i \equiv i \Delta x, \quad h(x) \Rightarrow h_i \equiv h(x_i), \quad i = -\left(\frac{N}{2} - 1\right), \dots, -1, 0, 1, \dots, \frac{N}{2} \quad (13)$$

$$f \Rightarrow f_j \equiv j \Delta f, \quad H(f) \Rightarrow H_j \equiv \frac{H(f_j)}{\Delta x}, \quad j = -\left(\frac{N}{2} - 1\right), \dots, -1, 0, 1, \dots, \frac{N}{2} \quad (14)$$

where $\Delta x \Delta f = 1/N$. We obtain the **Discrete Fourier Transform** equations:

$$H_j = \sum_{i=-(N/2-1)}^{N/2} h_i e^{i\frac{2\pi ij}{N}} \quad (\text{forward}) \quad (15)$$

$$h_i = \frac{1}{N} \sum_{j=-(N/2-1)}^{N/2} H_j e^{-i\frac{2\pi ij}{N}} \quad (\text{inverse}) \quad (16)$$

A.2. Surface Height

From Eq (1), we obtain:

$$PSD(f) = \frac{2}{L} \left| \int_{-L/2}^{L/2} e^{i2\pi x f} h(x) dx \right|^2 \Rightarrow \sqrt{\frac{PSD(f) L}{2}} = \left| \int_{-L/2}^{L/2} e^{i2\pi x f} h(x) dx \right| \quad (17)$$

Here $PSD(f)$ is a real continuous function of the spatial frequency f . We first need to convert Eq (17) to a discrete Fourier transform. Using the equations in A.1 and relation $L = N\Delta x = 1/\Delta f$, we obtain:

$$|H_j| = \frac{|H(f_j)|}{\Delta x} = \frac{1}{\Delta x} \sqrt{\frac{PSD(f_j) L}{2}} = N \sqrt{\frac{PSD(f_j) \Delta f}{2}} = \left| \sum_{i=-(N/2-1)}^{N/2} h_i e^{i\frac{2\pi ij}{N}} \right| \quad (18)$$

Therefore H_j can be expressed as the forward Fourier transform of h_i as

$$H_j = N \sqrt{\frac{PSD(f_j) \Delta f}{2}} e^{i\varphi_j} = \sum_{i=-(N/2-1)}^{N/2} h_i e^{i\frac{2\pi ij}{N}} \quad (19)$$

Hence the surface height, $h(x_i) = h_i$, can be expressed as the inverse Fourier transform of H_j

$$h_i = \frac{1}{N} \sum_{j=-(N/2-1)}^{N/2} H_j e^{-i\frac{2\pi ij}{N}} = \frac{1}{N} \sum_{j=-(N/2-1)}^{N/2} N \sqrt{\frac{PSD(f_j) \Delta f}{2}} e^{i\varphi_j} e^{-i\frac{2\pi ij}{N}} \quad (20)$$

where φ_j is a random phase factor. A set of surface heights, h_i , can be generated from a set of phase factor φ_j . Therefore for a given PSD, we can generate as many sets of surface map (of the same roughness) as we want by changing the random phase factor φ_j . Because h_i , the surface height, has to be real, this requires $H_{-j} = H_j^*$, i.e. $PSD(f_{-j}) = PSD(f_j)$ and $\varphi_{-j} = -\varphi_j$.

A.3. Surface Tangent

Since

$$h_i = \frac{1}{N} \sum_{j=-(N/2-1)}^{N/2} H_j e^{-i\frac{2\pi j}{N} x} = \frac{1}{N} \sum_{j=-(N/2-1)}^{N/2} H_j e^{-i2\pi x_i f_j} \quad (21)$$

The surface tangent can be obtained by taking the derivative on both sides of Eq. (21) with respect to x_i :

$$h'_i = \frac{1}{N} \sum_{j=-(N/2-1)}^{N/2} (-i2\pi f_j H_j) e^{-i2\pi x_i f_j} = \frac{1}{N} \sum_{j=-(N/2-1)}^{N/2} (-i2\pi f_j H_j) e^{-i\frac{2\pi j}{N} x} \quad (22)$$

The surface tangent h'_i also has to be real. This condition is automatically satisfied because

$$-i2\pi f_{-j} H_{-j} = -i2\pi(-f_j) H_j^* = i2\pi f_j H_j^* = (-i2\pi f_j H_j)^* \quad (23)$$

APPENDIX B. KIRCHHOFF SOLUTION

The wave scattering from random rough surfaces is described by the Kirchhoff solution² and its far-field approximation.

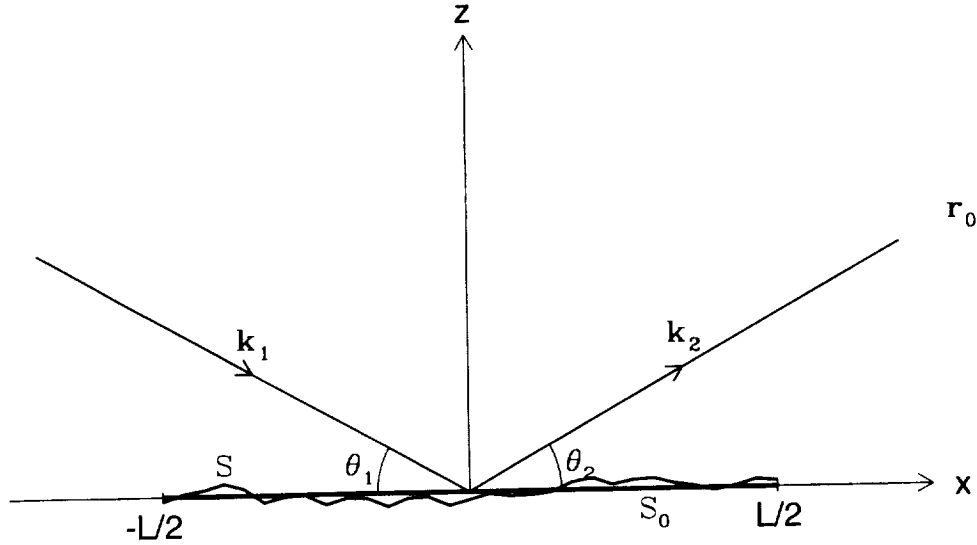


Figure 7. Wave scattering from a random rough surface. A flat surface S_0 with $z = 0$ lies in the x - y plane (y -axis not shown). A rough surface S has surface height $z = h(x, y)$, deviates from S_0 . The z axis is normal to the x - y plane and points up. Incident and reflecting (or scattering) wave-vectors are shown as \mathbf{k}_1 and \mathbf{k}_2 . Incident and reflecting grazing angles with respect to the surface S_0 are θ_1 and θ_2 . \mathbf{r}_0 is the observation point where the scattering is to be measured.

As shown in Figure 7, define:

- S_0 — 2-dimensional flat surface at $z = 0$.
- S — 2-dimensional rough surface, described by its surface height $z = h(x, y)$.
- $\mathbf{E}_1 e^{i\mathbf{k}_1 \cdot \mathbf{r}} = \mathbf{E}_1 e^{i(k_1 x + k_3 z)}$ — incident plane wave (in the incident plane, therefore $k_2 = 0$).
- $\mathbf{E}_2 e^{i\mathbf{k}_2 \cdot \mathbf{r}} = \mathbf{E}_2 e^{i(k_2 x + k_y y + k_z z)}$ — reflected or scattered wave from the rough surface S .
- θ_1, θ_2 — incident and reflecting grazing angles with respect to the surface S_0 .

where \mathbf{k}_1 and \mathbf{k}_2 are the wave vectors of the incident and scattered waves, so $\mathbf{E}_1 \cdot \mathbf{k}_1 = 0$, $\mathbf{E}_2 \cdot \mathbf{k}_2 = 0$, and

$$k \equiv \frac{2\pi}{\lambda} = |\mathbf{k}_1| = \sqrt{k_1^2 + k_3^2} = |\mathbf{k}_2| = \sqrt{k_x^2 + k_y^2 + k_z^2} \quad (24)$$

A vector normal to the local surface on S is given by:

$$\mathbf{n} = -\nabla(h(x, y) - z) = -\frac{\partial h(x, y)}{\partial x} \hat{\mathbf{x}} - \frac{\partial h(x, y)}{\partial y} \hat{\mathbf{y}} + \hat{\mathbf{z}} \quad (25)$$

The field at an observation point \mathbf{r}_0 is given by the integration of contributions from the field $\mathbf{E}(s)e^{i(k_1x+k_3z)}$ on the surface S :

$$\mathbf{E}(\mathbf{r}_0) = \frac{1}{i\lambda} \iint_S ds \mathbf{E}(s) e^{i(k_1x+k_3z)} \frac{e^{ikr}}{r^2} (\hat{\mathbf{n}} \cdot \mathbf{r}) = \frac{1}{i\lambda} \iint dx dy \mathbf{E}(s) e^{i(k_1x+k_3h(x,y))} \frac{e^{ikr}}{r^2} (\mathbf{n} \cdot \mathbf{r}) \quad (26)$$

where ds is an element of surface area; $\mathbf{E}(s)$ is given by the incident wave \mathbf{E}_1 multiplied by the suitable reflection coefficient; the vector \mathbf{r} goes from the point of integration (x, y, z) to the observation point (x_0, y_0, z_0) , and $r = |\mathbf{r}|$; $\hat{\mathbf{n}}$ is a unit vector in the direction of \mathbf{n} , and $(\hat{\mathbf{n}} \cdot \mathbf{r}) ds = (\mathbf{n} \cdot \mathbf{r}) dx dy$. Eq. (26) is known as the general Kirchhoff solution for the wave scattering.

Next we derive the far-field approximation of this solution. When the reflecting surface is near the origin of the coordinate system and the observation point is far from the origin, i.e. when $(x \ll x_0, y \ll y_0, z \ll z_0)$, we have:

$$\mathbf{k}_2 = k_x \hat{\mathbf{x}} + k_y \hat{\mathbf{y}} + k_z \hat{\mathbf{z}} = k \frac{(x_0 - x)}{|\mathbf{r}|} \hat{\mathbf{x}} + k \frac{(y_0 - y)}{|\mathbf{r}|} \hat{\mathbf{y}} + k \frac{(z_0 - z)}{|\mathbf{r}|} \hat{\mathbf{z}} \approx \frac{k}{r_0} (x_0 \hat{\mathbf{x}} + y_0 \hat{\mathbf{y}} + z_0 \hat{\mathbf{z}}) \quad (27)$$

$$\mathbf{r} = (x_0 - x) \hat{\mathbf{x}} + (y_0 - y) \hat{\mathbf{y}} + (z_0 - z) \hat{\mathbf{z}} \approx x_0 \hat{\mathbf{x}} + y_0 \hat{\mathbf{y}} + z_0 \hat{\mathbf{z}} \approx \frac{r_0}{k} (k_x \hat{\mathbf{x}} + k_y \hat{\mathbf{y}} + k_z \hat{\mathbf{z}}) \quad (28)$$

$$r = |\mathbf{r}| = \sqrt{(x_0 - x)^2 + (y_0 - y)^2 + (z_0 - z)^2} \approx r_0 - \frac{x_0}{r_0} x - \frac{y_0}{r_0} y - \frac{z_0}{r_0} z \quad (29)$$

where $r_0 = |\mathbf{r}_0| = \sqrt{x_0^2 + y_0^2 + z_0^2}$. Keep the first order of r in the phase factor and zeroth order elsewhere:

$$\mathbf{n} \cdot \mathbf{r} \approx -\frac{r_0}{k} \left[k_x \frac{\partial h(x, y)}{\partial x} + k_y \frac{\partial h(x, y)}{\partial y} - k_z \right] \quad (30)$$

$$e^{ikr} \approx e^{ik(r_0 - \frac{x_0}{r_0} x - \frac{y_0}{r_0} y - \frac{z_0}{r_0} z)} \approx e^{ikr_0} e^{-i(k_x x + k_y y + k_z h(x, y))} \quad (31)$$

Eq. (26) becomes:

$$\mathbf{E}(\mathbf{r}_0) \approx -\frac{1}{i\lambda} \iint dx dy \mathbf{E}(s) e^{i(k_1x+k_3z)} \frac{e^{ikr_0}}{r_0^2} e^{-i(k_x x + k_y y + k_z z)} \frac{r_0}{k} \left[k_x \frac{\partial h(x, y)}{\partial x} + k_y \frac{\partial h(x, y)}{\partial y} - k_z \right] \quad (32)$$

$$= \frac{ie^{ikr_0}}{2\pi r_0} \iint dx dy \mathbf{E}(s) e^{i(k_1x+k_3h(x,y))} e^{-i(k_x x + k_y y + k_z h(x,y))} \left[k_x \frac{\partial h(x, y)}{\partial x} + k_y \frac{\partial h(x, y)}{\partial y} - k_z \right] \quad (33)$$

$$= \frac{ie^{ikr_0}}{2\pi r_0} \iint dx dy \mathbf{E}(s) e^{i[(k_1-k_x)x - k_y y + (k_3-k_z)h(x,y)]} \left[k_x \frac{\partial h(x, y)}{\partial x} + k_y \frac{\partial h(x, y)}{\partial y} - k_z \right] \quad (34)$$

This is the far-field approximation of the Kirchhoff solution for the wave scattering.

APPENDIX C. SCATTERING FORMULA

In this section, we derive the scattering formula from the Kirchhoff solution for the constructed model surfaces.

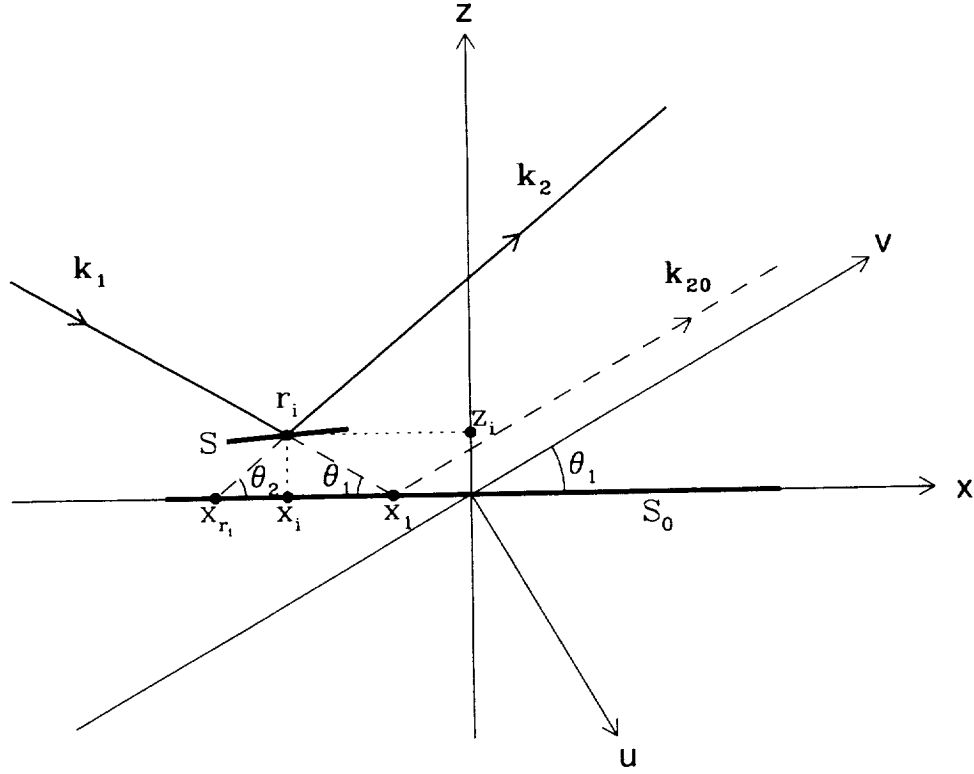


Figure 8. The scattering geometry. The flat surface S_0 is located on the x axis. The z axis is normal to the surface S_0 . The u - v axes form a coordinate system that is rotated clockwise from the x - z axes by $(\frac{\pi}{2} - \theta_1)$, so the v axis is aligned with the specular reflection direction. An incident ray, \mathbf{k}_1 , comes in from the left with a grazing angle θ_1 ; had it struck the surface S_0 at x_1 , it would have been reflected parallel to the v axis as \mathbf{k}_{20} . However, it actually strikes the rough surface S at $r_i(x_i, z_i)$, and is reflected at an angle θ_2 as \mathbf{k}_2 . The intersection of \mathbf{k}_2 with the surface S_0 is at x_{r_1} .

C.1. Integral on 1-dimensional flat surface S_0

We first reduce the Kirchhoff solution to a 1-dimensional integral on flat surface S_0 . Consider:

- In plane scattering: $k_y = 0$
- One dimensional surface, i.e. $h(x, y)$ only depends on x : $h(x, y) = h(x)$

Eq. (33) becomes:

$$\mathbf{E}(\mathbf{r}_0) = \frac{ie^{ikr_0}}{2\pi} \int dx \mathbf{E}(s) e^{i(k_1 x + k_3 h(x))} e^{-i(k_x x + k_z h(x))} \left[k_x \frac{\partial h(x)}{\partial x} - k_z \right] \quad (35)$$

here we have omitted a dimensionless factor $a = Y/r_0$, where Y is the transverse surface dimension; this factor will be absorbed later in an overall normalization factor \mathcal{A} .

Figure 8 shows the scattering geometry. The incident ray, \mathbf{k}_1 , strikes the rough surface at $r_i(x_i, z_i)$ and is reflected as \mathbf{k}_2 , where x_i is one of the N positions of the constructed model surface (see Appendix A) and $z_i = h(x_i) = h_i$. The reflected field at r_i is

$$\mathbf{E}(r_i) e^{i(k_1 x_i + k_3 z_i)} = \mathbf{E}(x_i, h_i) e^{i(k_1 x_i + k_3 h_i)} \quad (36)$$

For the integral (35), this is equivalent to have a field at $(x_{r_i}, 0)$, the intersection of \mathbf{k}_2 and \mathbf{x} axis, on the surface S_0 described by:

$$\mathbf{E}(x_{r_i}, 0) = \mathbf{E}(r_i) e^{i(k_1 x_i + k_3 h_i - k h_i / \sin \theta_2)} \quad (37)$$

where $k h_i / \sin \theta_2$ is the phase delay between (x_i, h_i) and $(x_{r_i}, 0)$. Let:

$$\mathbf{E}(x_{r_i}) = \mathbf{E}(x_{r_i}, 0) e^{-i k_1 x_{r_i}} = \mathbf{E}(r_i) e^{i(k_1 x_i + k_3 h_i - k h_i / \sin \theta_2 - k_1 x_{r_i})} = \mathbf{E}(r_i) e^{i \phi_i} \quad (38)$$

So the integral (35) can be written as

$$\mathbf{E}(\mathbf{r}_0) = \frac{i e^{i k r_0}}{2\pi} \int dx \mathbf{E}(x) e^{i(k_1 x - k_x x - k_z h(x))} \left[k_x \frac{\partial h(x)}{\partial x} - k_z \right] \quad (39)$$

Now the integration boundary has changed from $\mathbf{E}(s)$ on the rough surface S to $\mathbf{E}(x)$ on the flat surface S_0 , so $h(x) = 0$ and $\frac{\partial h(x)}{\partial x} = 0$. Therefore Eq. (39) becomes:

$$\mathbf{E}(\mathbf{r}_0) = \mathbf{E}(k_x, k_z) = \frac{i e^{i k r_0}}{2\pi} \int dx \mathbf{E}(x) e^{i(k_1 - k_x)x} (-k_z) = -\frac{i k_z e^{i k r_0}}{2\pi} \int dx \mathbf{E}(x) e^{i(k_1 - k_x)x} \quad (40)$$

here the reflected field $\mathbf{E}(x)$ are calculated at non-uniformly distributed, discrete points $x = x_{r_i}$. The position, x_{r_i} , and the phase, ϕ_i , of the field $\mathbf{E}(x_{r_i})$ are:

$$x_{r_i} = x_i - \frac{h_i}{\tan \theta_2} \quad (41)$$

$$\begin{aligned} \phi_i &= k_1 x_i + k_3 h_i - \frac{k h_i}{\sin \theta_2} - k_1 x_{r_i} = k \left(\cos \theta_1 x_i - \sin \theta_1 h_i - \frac{h_i}{\sin \theta_2} - \cos \theta_1 \left(x_i - \frac{h_i}{\tan \theta_2} \right) \right) \\ &= -k h_i \left(\sin \theta_1 + \frac{1}{\sin \theta_2} - \frac{\cos \theta_1}{\tan \theta_2} \right) = -k h_i \frac{1 - \cos(\theta_1 + \theta_2)}{\sin \theta_2} = -2 k h_i \frac{\sin^2 \frac{\theta_1 + \theta_2}{2}}{\sin \theta_2} \end{aligned} \quad (42)$$

where $k_3 = -k \sin \theta_1$, because, by definition, the \mathbf{z} axis points up.

Thus for the field $\mathbf{E}(s)$ of each ray \mathbf{k}_1 at r_i , we can use its equivalent field $\mathbf{E}(x)$ at x_{r_i} to do the integral ($x_{r_i} < x_i$ when $h_i > 0$, $x_{r_i} > x_i$ when $h_i < 0$).

C.2. Fourier transform with variable ξ

Define a coordinate system $\mathbf{u}-\mathbf{v}$ that is rotated clockwise from the $\mathbf{x}-\mathbf{z}$ axes by $(\frac{\pi}{2} - \theta_1)$, so the \mathbf{v} axis is aligned with the specular reflection direction (see Figure 8). Define the scattering angle, θ , as the angle of deviation clockwise from the \mathbf{v} axis, i.e. $\theta = \theta_1 - \theta_2$. Also define the variable $\xi = \frac{k_1 - k_x}{2\pi}$. Therefore:

$$k_1 = k \cos \theta_1, \quad k_x = k \cos \theta_2 = k \cos(\theta_1 - \theta), \quad k_z = k \sin \theta_2 = k \sin(\theta_1 - \theta) \quad (43)$$

$$2\pi \xi = k_1 - k_x = k \cos \theta_1 - k \cos(\theta_1 - \theta) = -2 k \sin(\theta_1 - \frac{\theta}{2}) \sin \frac{\theta}{2} \quad (44)$$

$$\theta = \theta_1 - \cos^{-1} \left(\cos \theta_1 - \frac{2\pi \xi}{k} \right) = \theta_1 - \cos^{-1} (\cos \theta_1 - \xi \lambda) \quad (45)$$

The scattering equation (40) becomes:

$$\mathbf{E}(\mathbf{r}_0) = \mathbf{E}(\xi(\theta)) = -\frac{i e^{i k r_0} k \sin(\theta_1 - \theta)}{2\pi} \int dx \mathbf{E}(x) e^{i 2\pi \xi x} = -\frac{i e^{i k r_0} \sin(\theta_1 - \theta)}{\lambda} \int dx \mathbf{E}(x) e^{i 2\pi \xi x} \quad (46)$$

Thus, the scattering field $\mathbf{E}(\xi)$ can be obtained from the Fourier transform integral of the field $\mathbf{E}(x)$ on the surface S_0 . And it can be expressed as $\mathbf{E}(\theta)$ using Eq. (44).

C.3. Discrete Fourier transform at x_i

In practice, this integral is performed numerically using the Fast Fourier Transform (FFT) on N uniformly distributed points x_i 's where we constructed the model surface. Therefore we need to convert the field $\mathbf{E}(x_{r_i})$ to the field $\mathbf{E}(x_i)$. This can be simply done by multiplying $\mathbf{E}(x_{r_i})$ with two factors:

$$\mathbf{E}(x_i) = A_i B_i \mathbf{E}(x_{r_i}) = A_i B_i \mathbf{E}\left(x_i - \frac{h_i}{\tan \theta_2}\right) = A_i B_i \mathbf{E}(r_i) e^{i\phi_i} \quad (47)$$

Where the factor A_i is used to adjust the incident plane wave density due to the different surface height h_i 's at the uniform grid x_i 's; it is calculated by intercepting all the incident rays that strike on the surface S at (x_i, h_i) 's with a coordinate that is perpendicular to the direction of incidence. Let the intercepting points be w_i 's on the coordinate. Then:

$$A_i = \frac{w_{i+1} - w_{i-1}}{2 \Delta x \sin \theta_1} \quad (48)$$

The factor B_i is used to adjust the outgoing ray density due to the redistribution of the reflected rays from the non-uniform grid x_{r_i} to the uniform grid x_i . For example, when the point x_{r_i} falls between the fixed grid points x_{i-1} and x_i ($x_i - x_{i-1} = \Delta x$), then

$$\frac{x_i - x_{r_i}}{\Delta x} \mathbf{E}(x_{r_i}) \text{ is added to field } \mathbf{E}(x_{i-1}) \quad (49)$$

$$\frac{x_{r_i} - x_{i-1}}{\Delta x} \mathbf{E}(x_{r_i}) \text{ is added to field } \mathbf{E}(x_i) \quad (50)$$

This process is done for each ray until all the fields are redistributed to the uniform grid x_i .

Having obtained the field $\mathbf{E}(x_i)$ on uniform grid, x_i , we can rewrite the scattering equation (46) as the discrete Fourier transform (see Appendix A.1). Let:

$$x \Rightarrow x_i \equiv i \Delta x, \quad \mathbf{E}(x) \Rightarrow \mathbf{E}_i \equiv \mathbf{E}(x_i), \quad i = -\left(\frac{N}{2} - 1\right), \dots, -1, 0, 1, \dots, \frac{N}{2} \quad (51)$$

$$\xi \Rightarrow \xi_j \equiv j \Delta \xi, \quad \mathbf{E}(\xi) \Rightarrow \mathbf{E}_j \equiv \frac{\mathbf{E}(\xi_j)}{\Delta x}, \quad j = -\left(\frac{N}{2} - 1\right), \dots, -1, 0, 1, \dots, \frac{N}{2} \quad (52)$$

where $\Delta x \Delta \xi = 1/N$. The scattering equation (46) becomes:

$$\mathbf{E}_j \equiv \frac{\mathbf{E}(\xi_j)}{\Delta x} = -\frac{e^{ikr_0} \sin(\theta_1 - \theta_j)}{\lambda} \sum_{i=-(N/2-1)}^{N/2} \mathbf{E}_i e^{i\frac{2\pi ij}{N}} \quad (53)$$

where

$$\mathbf{E}_i = \mathbf{E}(x_i) = A_i B_i \mathbf{E}(r_i) e^{i\phi_i} = A_i B_i \mathbf{E}_1 R(\theta_1 + \tan^{-1}(h'_i)) e^{i\phi_i} \quad (54)$$

where $R(\theta_1 + \tan^{-1}(h'_i))$ is the reflection coefficient of ray i with the local grazing angle, $\theta_1 + \tan^{-1}(h'_i)$, on the rough surface S . h'_i is the local surface tangent of the model surface.

The scattering intensity, I , is given as a function of the scattering angle, θ , by:

$$I(\theta_j) = I(\xi(\theta_j)) \equiv \mathcal{A} \mathbf{E}(\xi_j) \mathbf{E}^*(\xi_j) = \mathcal{A} \left(\frac{\Delta x \sin(\theta_1 - \theta_j)}{\lambda} \right)^2 \left| \sum_{i=-(N/2-1)}^{N/2} \mathbf{E}_i e^{i\frac{2\pi ij}{N}} \right|^2 \quad (55)$$

where \mathcal{A} is a normalization factor which we will derive in section C.5.

C.4. Scattering formula – the Fraunhofer diffraction pattern

With the Eq. (55), it seems that we can finally obtain the profile of scattering from the rough surface. However, this is not quite true, because of the discrete Fourier transform. The main disadvantage of the discrete Fourier transform is (what else?) “discrete”. Its shortcomings are displayed perfectly in this case. Eq. (55) is correct, but all of the points except the central peak ($\theta_j = 0$) are calculated in the valleys of the Fraunhofer diffraction pattern at:

$$\theta_j = -\frac{j \lambda}{N \Delta x \sin \theta_1} = -\frac{j \lambda}{L \sin \theta_1}, \quad j = \pm 1, \pm 2, \pm 3, \dots \quad (56)$$

where L is the surface length. In case of a perfect surface, Eq. (55) gives $I(\theta_j) = 0$ except for one point at $j = 0$, and the correct diffraction pattern from the finite surface length is not obtained. To get the diffraction patterns at angles between θ_j and θ_{j+1} , we divide $\theta_{j+1} - \theta_j$ into p equal spaces. The diffraction pattern at $\theta_{j+q/p}$ ($q < p$) can be calculated as:

$$I(\theta_{j+q/p}) = \mathcal{A} \left(\frac{\Delta x \sin(\theta_1 - \theta_{j+q/p})}{\lambda} \right)^2 \left| \sum_{i=-(N/2-1)}^{N/2} \mathbf{E}_i e^{i \frac{2\pi i(j+q/p)}{N}} \right|^2 \quad (q = 0, 1, 2, \dots, p-1) \quad (57)$$

$$= \mathcal{A} \left(\frac{\Delta x \sin(\theta_1 - \theta_{j+q/p})}{\lambda} \right)^2 \left| \sum_{i=-(N/2-1)}^{N/2} \left(\mathbf{E}_i e^{i \frac{2\pi i q/p}{N}} \right) e^{i \frac{2\pi i j}{N}} \right|^2 \quad (58)$$

So instead of one Fourier transform equation on \mathbf{E}_i , we need do p Fourier transform equations on $\mathbf{E}_i e^{i \frac{2\pi i q/p}{N}}$. Usually, $p = 8$ is sufficient to calculate very nice Fraunhofer diffraction patterns. Eq. (58) is the final scattering formula. It maps the field on the surface, $\mathbf{E}(\mathbf{x})$, to the field intensity of scattering, $I(\theta)$.

C.5. Normalization

Now let's derive the normalization factor \mathcal{A} introduced in Eq. (55). Let ε be the energy carried by each of the N incident rays of the plane wave \mathbf{E}_1 . The total incident energy, \mathcal{E}_i , total reflected energy on the surface, \mathcal{E}_r , and the total scattered energy, \mathcal{E}_s , are:

$$\mathcal{E}_i = N\varepsilon \quad (59)$$

$$\mathcal{E}_r = \sum_{i=-(N/2-1)}^{N/2} |\mathbf{E}_i|^2 = \varepsilon \sum_{i=-(N/2-1)}^{N/2} A_i^2 B_i^2 |R(\theta_1 + \tan^{-1}(h'_i))|^2 \quad (60)$$

$$\mathcal{E}_s = \int d\theta I(\theta) = \mathcal{A} \int d\xi |\mathbf{E}(\xi)|^2 \quad (61)$$

Define the reflectivity of the rough surface as:

$$\mathcal{R} \equiv \frac{\mathcal{E}_r}{\mathcal{E}_i} = \frac{1}{N} \sum_{i=-(N/2-1)}^{N/2} A_i^2 B_i^2 |R(\theta_1 + \tan^{-1}(h'_i))|^2 \quad (62)$$

Let $\mathcal{E}_r = \mathcal{E}_s$. We obtain:

$$\mathcal{A} = \frac{\varepsilon \sum_{i=-(N/2-1)}^{N/2} A_i^2 B_i^2 |R(\theta_1 + \tan^{-1}(h'_i))|^2}{\int d\xi |\mathbf{E}(\xi)|^2} = \frac{\varepsilon N \mathcal{R}}{\int d\xi |\mathbf{E}(\xi)|^2} = \frac{\mathcal{E}_i \mathcal{R}}{\int d\xi |\mathbf{E}(\xi)|^2} \quad (63)$$

ACKNOWLEDGMENTS

This work is supported by NASA Grant NAG8-1607.

REFERENCES

1. L. Rayleigh, *The Theory of Sound*, Macmillan, New York, 1877.
2. P. Beckmann and A. Spizzichino, *The Scattering of Electromagnetic Waves from Rough Surfaces*, Pergamon Press, Oxford, England, 1963.
3. J. A. Ogilvy, *Theory of Wave Scattering from Random Rough Surfaces*, IOP Publishing, Bristol, UK, 1991.
4. L. P. van Speybroeck, D. Jerius, R. J. Edgar, T. J. Gaetz, and P. Zhao, "Performance expectation versus reality," in *Grazing Incidence and Multilayer X-ray Optical Systems*, Hoover and Walker, eds., *Proc. SPIE* **3113**, p. 89, 1997.
5. P. Zhao, L. M. Cohen, and L. P. van Speybroeck, "AXAF HRMA mirror ring focus measurements," in *Grazing Incidence and Multilayer X-ray Optical Systems*, Hoover and Walker, eds., *Proc. SPIE* **3113**, p. 106, 1997.
6. P. Zhao *et al.*, "AXAF mirror effective area calibration using the C-continuum source and solid state detectors," in *X-Ray Optics, Instruments, and Missions*, Hoover and Walker, eds., *Proc. SPIE* **3444**, p. 234, 1998.
7. P. B. Reid, "Fabrication and predicted performance of the Advanced X-ray Astrophysics Facility mirror ensemble," in *X-ray and Extreme Ultraviolet Optics*, Hoover and Walker, eds., *Proc. SPIE* **2515**, p. 361, 1995.
8. P. Zhao and L. P. van Speybroeck, "AXAF VETA-I mirror x-ray test results cross check with the HDOS metrology data," in *X-ray and Extreme Ultraviolet Optics*, Hoover and Walker, eds., *Proc. SPIE* **2515**, p. 391, 1995.
9. cf. W. H. Press, S. A. Teukolsky, W. T. Vetterling, and B. P. Flannery, *Numerical Recipes in C: The Art of Scientific Computing*, Cambridge University Press, Cambridge, 1993.



